



Final Report

Processing and Properties of Alumina-Matrix Nanocomposites

By

Assist. Prof. Dr. Santi Maensiri et al.

December 2005





Final Report

Processing and Properties of Alumina-Matrix Nanocomposites

$\mathbf{B}\mathbf{y}$

Assist. Prof. Dr. Santi Maensiri et al.

December 2005

Final Report

Processing and Properties of Alumina-Matrix Nanocomposites

Researchers:

- 1. Asist. Prof. Dr. Santi Maensiri (Principal investigator)
- 2. Asist. Prof. Dr. Vittaya Amornkitbamrung (Mentor)

Department of Physics, Faculty of Science

Khon Kaen University, Khon Kaen, Thailand, 40002

Supported by

The Commission on Higher Education, The Ministry of Education and The

Thailand Research Funds

(ความเห็นในรายงานนี้เป็นของผู้วิจัย ทบวงฯ และ สกว. ไม่จำเป็นต้องเห็นด้วยเสมอไป)

CONTENTS

SECTION	PAGE
ACKNOWLEDGEMENT	
1. EXECUTIVE SUMMARY	1
2. SCIENTIFIC AND TECHNICAL DESCRIPTION	2
2.1 Introduction, significance of the problem	2
2.2 Experimental procedure	3
2.2.1 Materials fabrication, surface preparation and characterisation	3
2.2.1.1 Materials fabrication	3
2.2.1.1.1 Alumina-diamond nanocomposite	5
2.2.1.1.2 Alumina-carbon nanofibre nanocomposite	6
2.2.1.2 Surface preparation	6
2.2.1.3 Density measurement	7
2.2.1.4 Microstructure and grain size measurement	7
2.2.1.5 X-ray diffraction	8
2.2.1.6 Raman spectroscopy	8
2.2.2 Mechanical properties	8
2.2.2.1 Young's modulus	8
2.2.2.2 Hardness and fracture toughness	11
2.2.2.3 Fracture strength	12
2.2.3 Thermoelectric power	14
2.3 Results and discussion	15
2.3.1 Alumina-diamond nanocomposite	15
2.3.2 Alumina-carbon nanofibe nanocomposites	17
2.3.2.1 Structure	17
2.3.2.2 Microstructure and mechanical properties	18
2.3.2.3 Thermoelectric power	24
2.4 Conclusions	27
2.5 References	28
3. OUTPUT	31
4. APPENDICES	
A. Manuscript 1	
B. Manuscript 2	

ACKNOWLEDGEMENT

We are graceful to Prof. Shigetaga Wada of Chulalongkorn University for providing the hot press facilities.

We also thank the following institutions for providing research facilities:

- Thailand Institute of Scientific and Technological Research (TISTR) for providing Instron Testing machine and thermoelectric properties measurement facilities.
- National Metal and Materials Technology Center (MTEC) for providing elastic modulus measurement facilities.
- The Faculty of Science Electron Microscopy Unit for proving SEM facilities
- The Postgraduate Education Development (PED) in Physics Program, The Commission on Higher Education, The Ministry of Education, Thailand.
- Solid State Physics Laboratory, Department of Physics, Faculty of Science,
 Khon Kaen University for providing most of the research facilities.

This work is financially supported by the Thailand Research Fund (TRF), Thailand under the contract no. MRG4580012.

1. EXECUTIVE SUMMARY

Alumina (Al₂O₃), alumina reinforced with 5vol.% nanocrystalline diamond, and alumina reinforced with 1, 2.5 and 5vol.% carbon nanofiber (CNF) were fabricated by conventional powder processing route and followed by hot-pressing process. Structure, microstructure and mechanical properties of the hot-pressed materials were investigated. In alumina-diamond system, Raman spectroscopy revealed the transformation of the diamond to graphite in this system. However, no significant improvement in mechanical properties of the nanocomposite over the pure alumina has been observed. This was possibly due to the transformation of diamond to graphite phase occurs at high temperature. This transformation results in a low density with high porosity in the nanocomposite. Since only low density of ~ 78 was obtained in the alumina-diamond composite, the project was moved on to the alumina-carbon nanofiber system.

Microstructure of the alumina-carbon nanofiber nanocomposites was revealed by SEM and the grain size of the hot-pressed materials was in the range of 1.19-1.66 µm. Crystal structure of the powders and hot-pressed alumina and alumina/CNF nanocomposites were determined by XRD and Raman spectroscopy. Mechanical properties of the hot-pressed were evaluated by the measurements of Young's modulus, indentation hardness and fracture toughness, bending strength. The hardness of reinforced alumina-matrix nanocomposite decreased with increasing CNF volume fraction, whereas the fracture toughness was found to increase ~3-13% depending on the amount of CNF. The toughening mechanism is strongly related to the crack-bridging effect of CNF during the crack propagation in alumina/CNF nanocomposites. The strength of the nanocomposites dramatically decreases with increasing CNF volume fraction. The lower values of bending strength in the nanocomposites could be correlated to the lower density and agglomerates of CNF. Annealing at 1300°C in air for 2 h decreased the strength of ~20% in the alumina but caused the strength improvements as high as 33% in the nanocomposite reinforced with 5 vol.% CNF. The decrease in strength of alumina has been attributed to grain growth, whereas the increase in strength after annealing in the nanocomposite is attributed to crack healing in parallel with an oxidation reaction of the CNF, leading to a reduction in the surface flaw density and critical flaw size on annealing. It has been also found that alumina/CNF composites exhibit thermoelectric properties, suggesting potential for use as a promising thermoelectric material. This will be further investigated in the future.

Key words: Alumina; Nanocrystalline diamond; Carbon nanofiber; Nanocomposite; Hotpressing; Raman spectroscopy; Thermoelectric power

2. SCIENTIFIC AND TECHNICAL DESCRIPTION

2.1 Introduction, significance of the problem

Aluminum oxide or alumina (Al₂O₃), as one of the most common groups of advanced ceramics, has great potential to replace high-temperature metals and improve upon them in many demanding applications, especially for structural applications due to its high hardness, good wear resistance and chemical inertness. However, it suffers from low fracture toughness, strength degradation at high temperatures, and poor creep and thermal shock resistance. These drawbacks greatly limit its reliability in service [1, 2]. In 1991, Niihara [3] proposed the concept of structural ceramic nanocomposites in a review of their processing, microstructure and properties, based mainly on results obtained on the Al₂O₃/SiC and Si₃N₃/SiC systems. Alumina-matrix reinforced with either ceramic nanophases (e.g. SiC [3, 4, 5, 6, 7], diamond [8-12], ZrO₂ [13, 14], BaTiO₃ [15]), carbon nanotubes (e.g. single-walled carbon nanotube (SWNT) [16, 17], multi-walled carbon nanotube (MWNT) [18-21]) or metal nanophases (e.g. Nb [12], Ni [22], Cu [23], Cr [24]) have been reported to have a better room temperature mechanical properties over pure alumina. This indicates that industrial opportunities may exist for possible applications of the nanocomposite as wear parts, mechanical seals, and improved grinding grits [1, 5].

In recent years, carbon-based materials such as carbon nanotube, diamond, and carbon micro/nano-fibers have attracted much attention as fascinating nanomaterials not only because of their extraordinary physical and chemical properties but also because of their versatile potential applications [25]. Most recently, carbon fiber (CNF) [26] has been used as a reinforcement for composites in polymers [27-31], metal-matrix composites [32, 33] and ceramic-matrix composites [34-39] with improving properties over the unreinforced matrices. To the best of our knowledge, there has not yet been reports on systems of alumina-carbon nanofiber composite system and alumina-nanoparticulate diamond. This project will investigate new ceramic nanocomposite systems based entirely on alumina, primarily alumina-diamond and alumina-carbon nanofiber. The aim of the project is to study the processing and properties of alumina/diamond and alumina/carbon nanofibre nanocomposites. The project will involve the ceramic processing and fabrication, investigation of microstructure by scanning electron microscopy (SEM), mechanical properties testing.

2.2 Experimental procedure

This section presents the methods used for material fabrication and characterization, and results of mechanical property testing of hot-pressed alumina and alumina reinforced with diamond and carbon nanofiber.

2.2.1 Materials fabrication, surface preparation and characterisation

2.2.1.1 Materials fabrication

In this study, we used commercially available AES 11C alumina powder (Sumitomo Co., Japan) as the matrix and either a commercial diamond powder of average particle size of 3.2 nm (Nanostructured & Amorphous Materials, USA) or a commercial carbon nanofiber (CNF) powder of average outer diameter of 100-200 nm and 15-20 µm in length (Nanostructured & Amorphous Materials, USA) as the reinforcements to produce nanocomposite ceramics. Morphology of the diamond and CNF is shown in Figure 1.

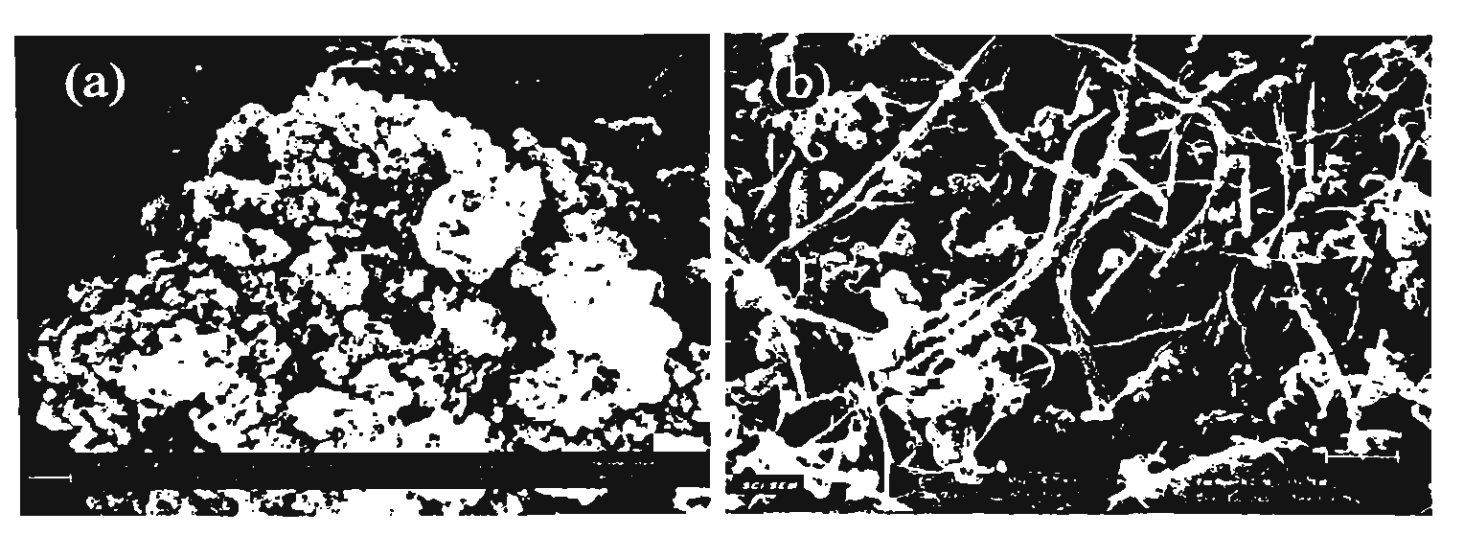


Figure 1. SEM micrographs of diamond nanopoders (a) and carbon nanofibers (b) used in this study.

Physical properties and chemical analyses of the powders, as given by the suppliers, are shown in Table 3.1. The amount of the powders needed to produce alumina/ 1, 2.5 and 5 vol% Carbon nanofiber nanocomposite and alumina/5vol.% nanodiamond (in lots of 100 g) was calculated using the expression in Equation (1) and is shown in Table 1.

% Reinforcement by weight =
$$\frac{V_C \rho_C}{V_C \rho_C + (1 - V_C) \rho_{AlpO_1}} x 100$$
 (1)

Here V_C is a percentage of reinforcement (i.e. diamond or carbon nanofiber) by volume; ρ_C density of reinforcement (3.52 g/cm³ for diamond and 1.90 g/cm³ for carbon nanofiber); $\rho_{Al_2O_3}$ density of the matrix Al_2O_3 (= 3.96 g/cm³). Theoretical densities of the nanocomposites were estimated from Equation (2) using the simple rule of mixtures:

$$\rho_{th} = \rho_{Al_2O_2} V_{Al_2O_2} + \rho_C V_C \tag{2}$$

Table 1. (a) Physical properties and (b) chemical analyses of AES 11 C alumina, diamond and carbon nanofibre powders (Data from supplier).

a) Physical properties

Material	Colour	Purity (%)	Mean Powder Particle Size (nm)	Specific Surface Area (m²/g)	Density (g/cm ³)	Crystal Structure
alumina	White	99.8	400	-	3.96	α
diamond	Beige-grey	95	3.2	278-335	3.52	-
CNF	Black	> 97	100-200 nm (outer diam.) 15-20 µm in length	200-450	1.90	-

b) Chemical Analyses (wt %)

Alumina	Al ₂ O ₃	SiO ₂	Fe ₂ O ₃	Na ₂ O	MgO	Cu
Alumina	99.8	0.04	0.01	0.04	0.05	0.02
diamond	N/A					
CNF			N/A			

Material	%vol. reinforcement	Weight of Reinforcement (g)	%wt.Al ₂ O ₃ (g)	Theoretical density, ρ_{th} (g/cm ³)
Al ₂ O ₃	0	0	100	3.9600
Al ₂ O ₃ /5vol% diamond	1	4.4693	95.5307	3.9390
Al ₂ O ₃ /1vol% CNF	1	0.4823	99.5168	3.9394
Al ₂ O ₃ /2.5vol% CNF	2.5	1.2153	98.7847	3.9085
Al ₂ O ₃ /5vol% CNF	5	2.4631	97.5369	3.8570

Table 2. The amount of the powders used to produce alumina-matrix nanocomposites.

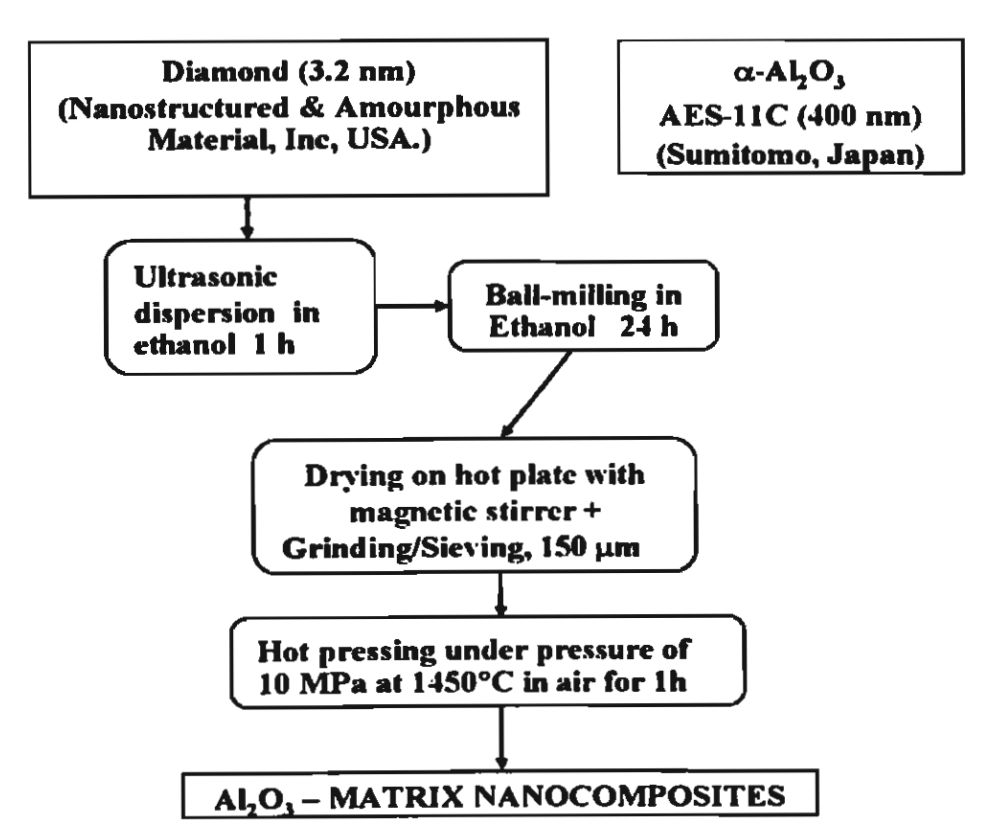


Figure 2. Schematic of the fabrication steps used for the preparation of the alumina and alumina-diamond nanocomposites.

2.2.1.1.1 Alumina-diamond nanocomposite

The materials fabricated in this study were hot-pressed alumina and alumina reinforced with 1, 2.5 and 5vol.% carbon nanofiber. The materials were produced in lots of 100 g as follows. A commercial diamond powder of average particle size of 3.2 nm was dispersed in 50 ml of ethanol and then ultrasonically agitated for 30 minutes. The diamond nanopowders

slurry was then added to α-Al₂O₃ powder of mean particle size ~400 nm in a ball mill with 150 ml of ethanol and zirconia milling media (diameter of 3 mm). After ball milling for 24 hours, the resultant slurry was dried. The dried powder was passed through a 150 μm sieve. The prepared composite powders were hot pressed at 10 MPa in a graphite die (55 cm in diameter) for 1h under argon. The hot pressing temperature was 1450°C. Pure alumina was fabricated using the same procedure but without any addition of diamond nanopowders. A schematic illustration of the conventional powder-processing route used in this work for alumina and nanocomposite powder production is shown in Figure 2.

2.2.1.1.2 Alumina-carbon nanofibre nanocomposite

The fabrication process of hot-pressed alumina reinforced with 1, 2.5 and 5vol.% carbon nanofiber was similar to that of the alumina-diamond nanocomposite except the use of carbon nanofiber instead of diamond nanopowder. Throughout this report, we assigned symbols of C1%, C2.5%, and C5% for alumina/1.0vol.%CNF, alumina/2.5vol.%CNF, and alumina/5.0vol.%CNF, respectively.

2.2.1.2 Surface preparation

Ceramics are both brittle and hard and these typical properties normally lead to a number of difficulties when preparing representative polished specimens. Damage is invariably introduced into a surface during preparation especially both cutting and grinding. The damage can take many forms including individual and/or multiple grain fracture, grain pull out, microcracking, dislocation glide and elastic stored energy. Therefore, careful selection of cutting, grinding and polishing procedures is required, and these must be optimised for each type of ceramic.

In this study, rectangular bar specimens of size about 40 mm x 4 mm x 3 mm for microstructural characterisation and mechanical properties evaluation were prepared in two surface-finishing conditions: "ground" surface, and a "fine polished" surface. Specimens were cut parallel to the grinding direction used. All four major faces of each specimen were subsequently machined and polished according to the procedures for ground surface or polished surface as follows. The specimens were ground with two grades of silicon carbide papers (no. 600 and 800). The polishing process, if used, was carried out after grinding using a Mecapol P260 automatic polishing machine (Presi, France). Four polishing steps were carried out using either diamond spray or diamond compounds. The first three polishing steps each removed at least 150 µm of material with diamond spray of 45 µm, 30 µm, and 15 µm

grit size. The third, fourth, and fifth steps removed smaller amounts of material (about 50 μ m) using 6 μ m, 3 μ m and 1 μ m diamond compounds. This procedure was used to completely remove the influence of surface grinding and should result in a surface whose properties are determined by the final polishing steps.

2.2.1.3 Density measurement

The sintered density measurements were made by the Archimedes method using deionised water as an immersion medium. Sintered densities were calculated based on the
"literature" densities of alumina (3.96 g/cm³) and the reinforcements (3.52 g/cm³ for
diamond, 1.90 g/cm³ for CNF). Samples were weighed dry, then boiled for at least 2 hours to
maximise penetration of water. After boiling, excess water from the sample surface was
removed with a wet tissue. Then "wet weight" measurements were taken. Finally, the
samples were weighed when immersed in de-ionised water. The densities are calculated
using the following formula:

$$\rho = \left(\frac{W_a}{W_w - W_i}\right) \rho_w \tag{3}$$

where ρ is relative density (g/cm³), W_a is dry weight in air (g), W_w is wet weight after boiling (g), W_i is immersed weight in water (g) and ρ_w is the density of water (0.99823 gcm⁻³ at room temperature).

2.2.1.4 Microstructure and grain size measurement

Polished surfaces of alumina and nanocomposite samples were etched in order to reveal the microstructure. Thermal etching was used for both alumina and nanocomposites. Thermal etching of alumina at 1450°C for 30 minutes in air easily revealed the microstructure. For nanocomposites, chemical etching was performed but it was not successful. Microstructures of all materials were characterised using Scanning Electron Microscopy (SEM) (LEO SEM VP1450). Mean grain size was evaluated using the standard linear intercept method [40]. A transparent grid containing several lines of known length was placed on the SEM micrograph of the thermally-etched polished surfaces. The number of intercepts between the test line and the grain boundaries was counted. For each specimen, the mean grain size obtained from counting at least 300 intercepts was calculated by:

$$D = 1.56 \times \left(\frac{L_{i}}{N \times M}\right) \tag{4}$$

where D is the mean grain size, N is number of intercepts along a grid line, L_i is intercept length and M is magnification of the micrograph. Pores were not counted and their length was always excluded from the L_i value.

2.2.1.5 X-ray diffraction

X-ray diffraction (XRD) was used for crystal phase identification of the starting powders and hot-pressed samples. The X-ray Diffraction measurements were performed on a Phillips X-ray difractometer (PW3710 mpd control, The Netherlands) with CuK α radiation ($\lambda = 0.15406$ nm).

2.2.1.6 Raman spectroscopy

The Raman spectra were performed at room temperature by using a triple spectrometer (Jobin Yvon/Atago-Bussan T-64000, France) with a liquid nitrogen cooled CCD detector for 800 s, in micro-mode. The Ar⁺ laser beam with the excitation $\lambda = 514.5$ nm was focused under 90x microscope objective and the laser spot size was between 1 and 2 μ m. Raman spectra were recorded in 2000–300 cm⁻¹ range. The spectral resolution was 1 cm⁻¹.

2.2.2 Mechanical properties

2.2.2.1 Young's modulus

Bulk elastic properties (Young's modulus, E, shear modulus, G, and Poisson's ratio, v) were measured by a resonance method using an MK5 "GrindoSonic" machine (J. W. Lemmens, Leuven, Belgium). It is based on the impulse excitation technique that was pioneered by Lemmens Electronika BV. This method measures the fundamental resonant frequency of test specimens of suitable geometry (for example, rectangular or disc specimens) by exciting them mechanically by a single elastic strike with an impulse tool. A transducer (for example, contact accelerometer or non-contacting microphone) senses the resulting mechanical vibrations of the specimen and transforms them into electrical signals. Specimen supports, impulse locations, and signal-pick up points are selected to induce and measure specific modes of the transient vibrations. The signals are analysed, and the fundamental resonant frequency is isolated and measured by a signal analyser. A transducer is used to pick up mechanical vibration. The analogue signal from the vibration detector is first fed to a twostage linear amplifier. A zero crossing detector marks off the signal periods. As soon as the peak detector senses that the incoming signal has started to decay, the successive period measurements commence. The MK5 "GrindoSonic" machine records all available periods and stores the results in the microprocessor memory for further analysis. When the incoming signal has died away, the processor selects the measurement corresponding to the preset and displays the result on the front panel. This test apparatus is shown in Figure 3. The appropriate fundamental resonant frequencies (see next section), dimensions, and density of the specimen are used to calculate the elastic properties of materials i.e. dynamic Young's modulus (E), dynamic shear modulus (G), and Poisson's ratio (v). In this study, two types of specimen shapes were used: rectangular bar and disc.

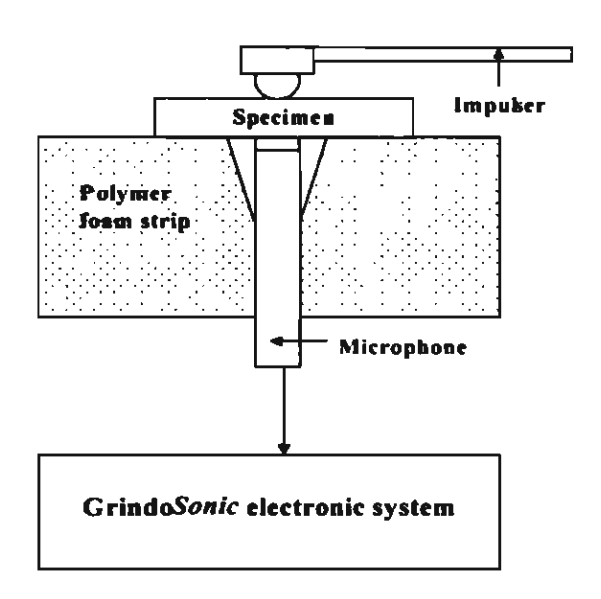


Figure 3. The apparatus set-up for impulse excitation technique. A specimen is positioned above a through-thickness hole in a soft polymer foam cushion. The specimen rests on the edges of the hole. In the hole, beneath the specimen a microphone is placed. The exciting impulse is imparted by lightly striking the specimen with an impulser (i.e. a small ceramic ball at the end of a flexible polymer strip). The signal is detected by the microphone and is stored and then analysed by the Grindo Sonic electronic system.

Rectangular bar specimens of size about 40 mm x 4 mm x 3 mm were used. Edges were sharp with no chamfer. A set of 8 specimens for each of alumina and nanocomposites was used for the measurement of E. The excitation is administered to the specimens in such a way as to favour the vibration mode as illustrated in Figure 4.

Note that only the fundamental flexure frequency was measured for a rectangular bar specimen because of the difficulty in the measurement of the fundamental torsion mode frequency due to limited specimen size. Therefore, only dynamic Young's modulus, E could

be determined from the rectangular bar specimens, according to the following equation [41, 42]:

$$E = 0.94642 \left(\frac{\rho f_f^2 L^4}{t^2} \right) A_f \tag{5}$$

where f_f is the fundamental resonant frequency (flexure mode) of a rectangular bar, L is the length, t is the thickness, ρ is the density of the specimen, and A_f is a correction factor to account for inertia effects and shearing given approximately [42] by:

$$A_{f} = 1 + 6.585(1 + 0.0752\nu + 0.8109\nu^{2})\left(\frac{t}{L}\right)^{2} - 0.868\left(\frac{t}{L}\right)^{4}$$

$$-\frac{8.340(1 + 0.2023\nu + 2.173\nu^{2})\left(\frac{t}{L}\right)^{4}}{1 + 6.338(1 + 0.14081\nu + 1.536\nu^{2})\left(\frac{t}{L}\right)^{2}}$$
(6)

Here, v is Poisson's ratio.

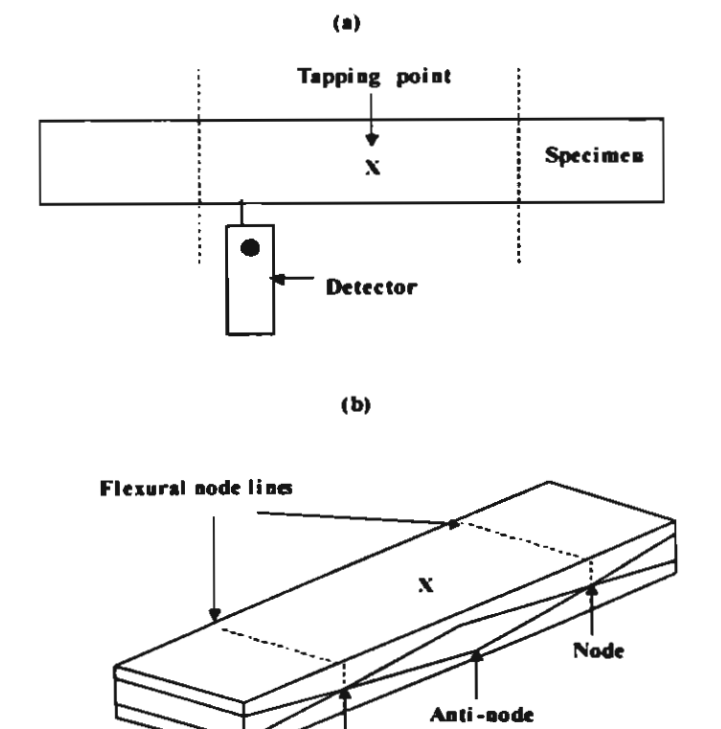


Figure 4. Schematic illustration of "Grindo Sonic" impulse excitation technique for flexural vibration mode of a rectangular bar, showing (a) top view and (b) side view.

2.2.2.2 Hardness and fracture toughness

The hardness and fracture toughness of materials were determined from the size of indentation and the length of cracks which develop during a Vickers indentation test and which can be measured optically at the specimen surface. The hardness, H (in GPa) is related to diagonal, d (in μ m) of the indentation and the contact load, P (in N), by the following equation:

$$H = 1854.4 \left(\frac{P}{d^2}\right) \tag{7}$$

The development of indentation fracture mechanics has allowed fracture toughness to be determined using the radial cracks that emanate from the hardness impression. In general, two major types of cracks are formed after a Vickers indentation: cracks perpendicular to the surface (these cracks are termed "median-radial cracks"); and "lateral cracks" that are approximately parallel to the surface. The former cracks are associated with the strength degradation caused by the contact event. The lateral cracks are associated with spalling and erosion that can occur during contact. Here we only consider the medial-radial cracks as they can be used to determine fracture toughness. Figure 5 shows cracking around indentation illustrating the indentation crack geometry. The fracture toughness or the critical stress intensity factor, K_{IC} (in MPa.m^{1/2}) can be determined using the following equation:

$$K_{KC} = \xi \left(\frac{E}{H}\right)^{1/2} \left(\frac{P}{c^{3/2}}\right) \tag{8}$$

Here H (in GPa) is the hardness determined at the load P (in N), E (in GPa) is Young's modulus and c (in m) is the radial crack length measured from the centre of the indentation impression. ξ is a material independent, dimensionless calibration constant which characterizes the geometry of the deformation field. Studies on many ceramics led to an average value of $\xi = 0.016 \pm 0.004$ [43].

In this study, a rectangular bar specimen of size about 40 mm x 4.0 mm x 3 mm of each material with 1 μ m polished finish on all sides was used for the test. The indentations were performed using a Vickers hardness testing machine (Hardness Tester, Model: DVK-2, Matsuzawa Seiki, Japan). Indentation loads of 50N with a holding time of 15 s for each indentation were used. The diagonal, d and radial crack length, c of at least 5 indentations for each load were measured using an optical microscope (Nikon, Japan). The average hardness for a given specimen type was used in calculations for Equation (7).

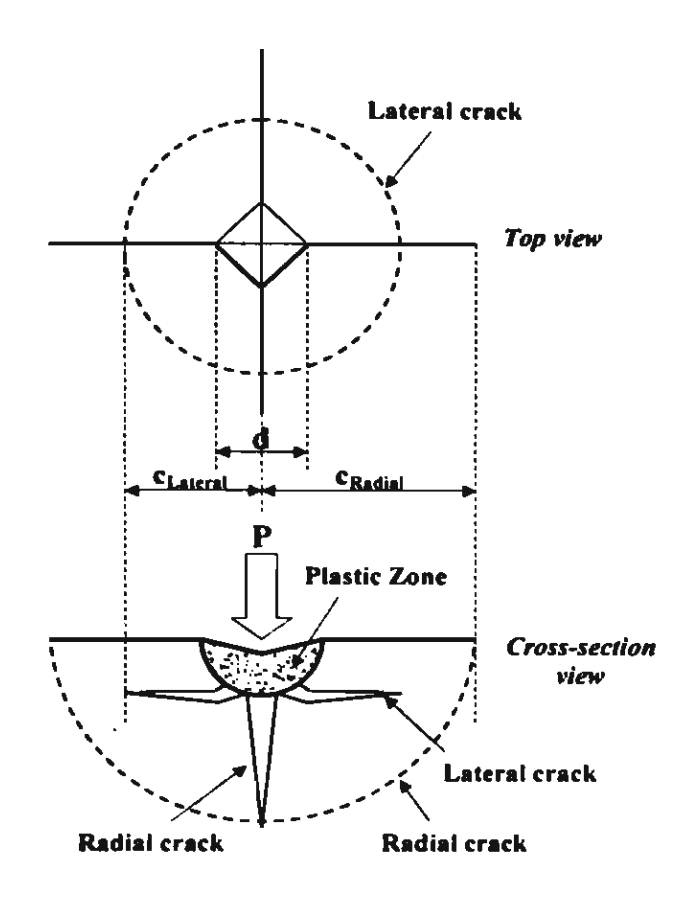


Figure 5. Schematic illustration of plastic zone and cracks formed by Vickers indentation in ceramic materials.

2.2.2.3 Fracture strength

The fracture strengths were measured using a 4-point bend test (flexure test) using rectangular bar specimens of size about 40 mm x 4.0 mm x 3 mm. Specimens were cut parallel to the grinding direction used. All four major faces of each specimen were subsequently machined and polished according to the procedures for ground surface as previously described in Section 2.2.1.2. The edges of the 'tensile' faces were bevelled and then polished with 1 µm diamond finished to reduce the effect of edge cracks. All tests were carried out on a conventional screw driven loading frame (Instron, Series IX Automated Materials Testing System), with a cross-head displacement speed of 0.5 mm/min, using a four-point bending rig with an inner span of 10 mm and an outer span of 30 mm.

Figure 6 schematically shows the flexure fixture used for the room-temperature strength measurement. According to the four-point loading geometry used to produce an applied moment in a rectangular specimen having a height h and width b, the fracture strength, σ_b , can be determined by

$$\sigma_f = \frac{My}{I} = \frac{3P_f(L_o - L_i)}{2bh^2} \tag{9}$$

where I is the second moment of inertia $(=bh^3/12)$, y is the distance from the neutral axis, P_f is the failure load, L_o is the outer load point span (=10 mm), and L_i is the inner load point span (=6 mm). The mean strength and standard deviation for each of the conditions studied was obtained using at least 5 specimens. For each specimen, b and h were measured using a standard micrometer to an accuracy of $\pm 0.01 \text{mm}$. The test was also done on the ground specimens annealed in air at 1300°C for 2h.

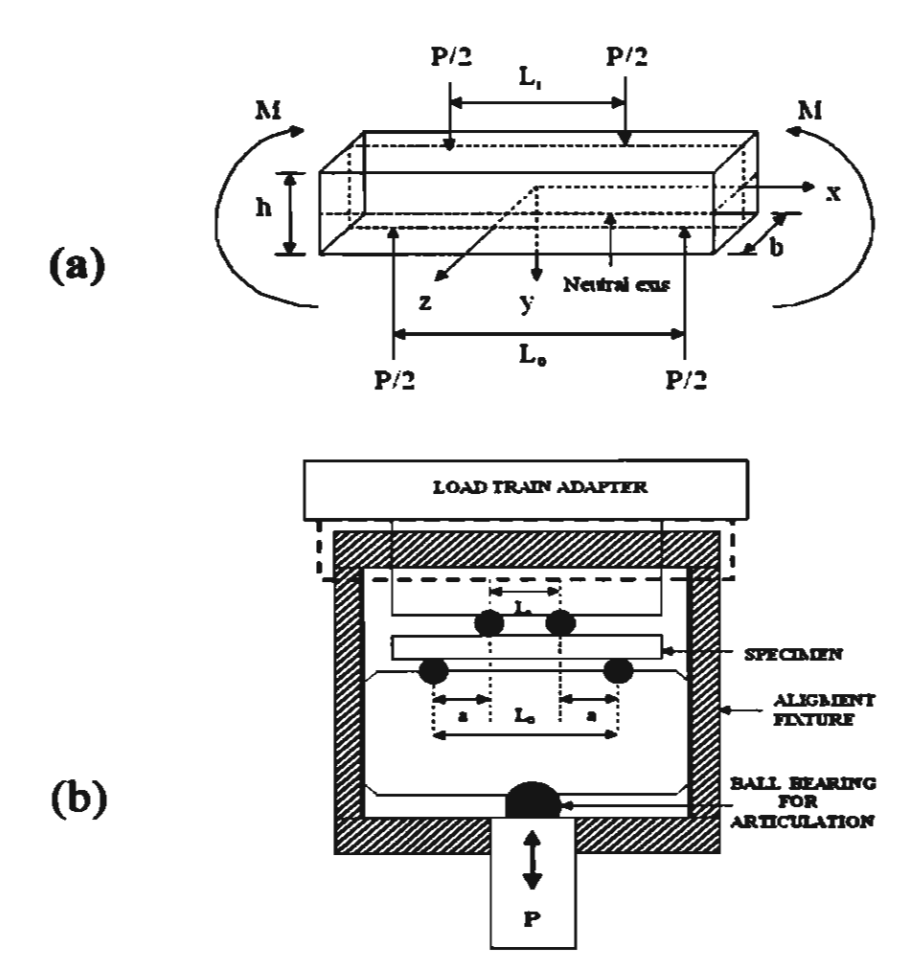


Figure 6. Four-point bending test.

- a) Schematic illustration of bending of a rectangular specimen.
- b) Flexure fixture used for measurement of room-temperature strength.

2.2.3 Thermoelectric power

The electrical resistivity (ρ) and Seebeck coefficient (S) were measured by an electrical resistivity-thermopower measuring device (ZEM-2, ULVAC Ltd.) in the temperature range from room temperature to about 1000 K. The power factor (P) was calculated from the measured Seebeck coefficient (S) and electrical resistivity (ρ), by the equation

$$P = \frac{S^2}{\rho} \tag{10}$$

In this study, a rectangular bar specimen of size about 20 mm x 4.0 mm x 3 mm of each material was used for the test.

2.3 Results and discussion

2.3.1 Alumina-diamond nanocomposite

The densities of the alumina and alumina/5vol.% diamond nanocomposite were 99.49% and 78.45% of theoretical density, respectively. The Raman spectra of the starting powders and hot-pressed materials are presented in Figure 9. Raman spectra of the alumina phase (Figure 9a and d) show typical peaks at around 379, 418, 645, 677 and 750 cm⁻¹. This is consistent with the results reported by Gallas et al. [44]. Raman spectra of the nanocrystalline diamond have a strong diamond peak at around 1325 cm⁻¹ accompanied by weak graphite peak (Figure 9b). In case of the hot pressed nanocomposite specimen (Figure 9e), there are no alumina peaks observed, but only two strong D and G peaks of graphite at around 1347 and 1585 cm⁻¹ are detected. The intensities of the Raman spectra of the alumina phase may be too low compared to those two peaks of the graphite phase. It is believed that the transformation of diamond to graphite phase occurs at high temperature. This transformation results in a low density with high porosity in the nanocomposite. It has been reported that graphitization of diamond depends on several factors, such as pressure, temperature, oxygen partial pressure, particle size, and diamond polytype [45]. In the present work, nano-sized diamond powders with high specific surface area and the low pressure used are likely to increase the graphitization in the nanocomposite.

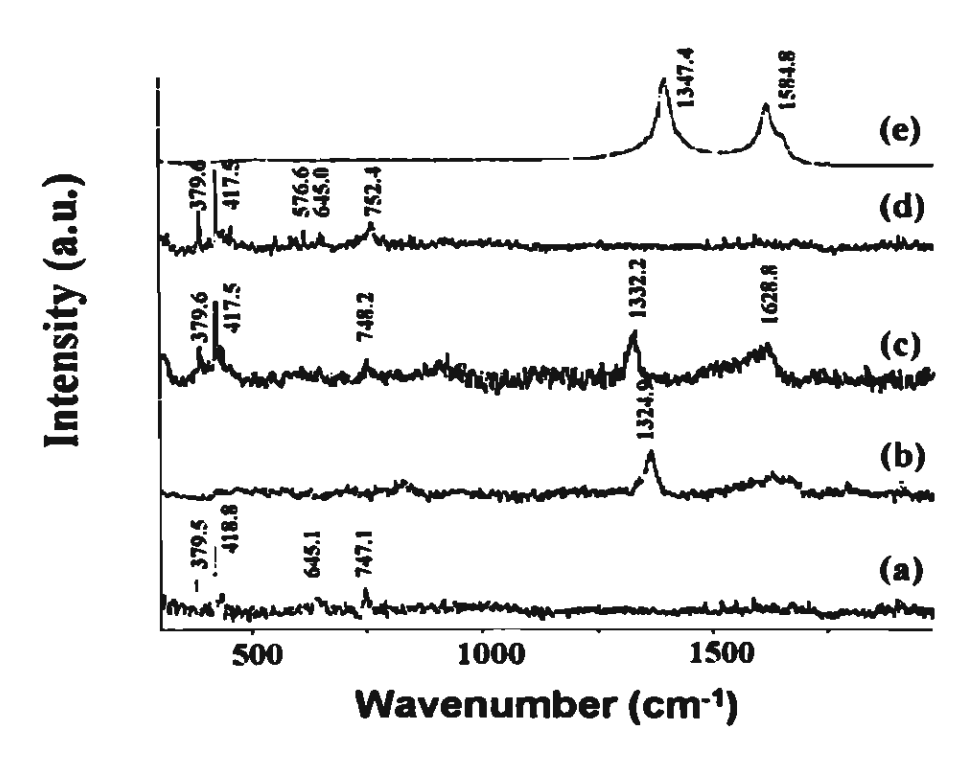


Figure 9. Raman spectra of alumina powder (a), diamond powder (b), alumina/5vol.% diamond powder (c), hot-pressed alumina (d), and hot-pressed alumina/5vol.% diamond (e).

For the determination of fracture toughness, the radial crack length, c of at least five indentations at each load was also measured. The hardness, H and fracture toughness, K_{IC} , was determined using Equations (7) and (8), respectively. In the calculations of K_{IC} , E values were calculated for the nanocomposites using strain compatibility model [46]:

$$E_{C} = \left[\frac{f_{m}}{E_{m}} + \frac{f_{p}}{E_{p}} - \frac{2f_{m}f_{p} \left(\frac{\nu_{m}}{E_{m}} - \frac{\nu_{m}}{E_{p}} \right)^{2}}{f_{p} \left(\frac{1 - \nu_{m}}{E_{m}} \right) + f_{m} \left(\frac{1 - \nu_{p}}{E_{p}} \right)} \right]^{-1}$$
(10)

where E, ν and f are Young modulus, Poison's ratio and volume fraction, respectively. c, m and p are for composite, matrix and particulate, respectively. The E value of 394 GPa was used for pure alumina [7], and this gives the E value of 800 GPa for the nanocomposite. The poison's ratio values of 0.24 and 0.20 are applied for the alumina and nanocomposite, respectively [47].

The average hardness and fracture toughness of the alumina and nanocomposite are presented in Table 3. The lower hardness in nanocomposite compared to the pure alumina was due to its low density and high porosity. No significant improvement in fracture toughness of the nanocomposite over the pure alumina has been observed.

Table 3 Summary of average hardness and fracture toughness of materials investigated

Materials	Hot-pressing temperature(°C)	Percent of theoretical	Hardness (GPa)	Fracture toughness (MPa.m ^{1/2})
alumina	1450	98.73 ± 0.25	19.1 ± 0.5	2.41 ±0.12
alumina/5vol.% diamond	1450	78.45 ± 0.64	3.4±0.3	3.13 ± 0.33

In summary, the hot-pressed alumina and alumina/5vol.% diamond nanocomposite were fabricated using conventional powder processing route. Hardness and fracture toughness of the materials were evaluated by the Vickers indentation technique. Raman spectroscopy is a useful technique for studying the phase compositions of the nanocomposites and it can reveal the transformation of the diamond to graphite in the alumina/diamond system. However, no significant improvement in mechanical properties of the nanocomposite over the pure alumina

has been observed. This was possibly due to the transformation of diamond to graphite phase occurs at high temperature. This transformation results in a low density with high porosity in the nanocomposite.

2.3.2 Alumina-carbon nanofibe nanocomposites

2.3.2.1 Structure

Figure 10 shows the XRD patterns of the starting powders, nanocomposite powders and hot-pressed samples of the alumina and alumina/CNF nanocomposites. The CNF powder has two XRD peaks near $2\theta = 26$ and 44° corresponding to the (002) and (100) layers of the graphite structure [48], whereas the alumina powder shows a typical XRD pattern of α -alumina phase. All the main XRD peaks of all the composite powders and hot-pressed samples are comparable to those of the powder diffraction pattern of α -alumina in the JCODS card no. 42-1468, and no graphite phase was detected due to the high crystallinity of α -alumina phase.

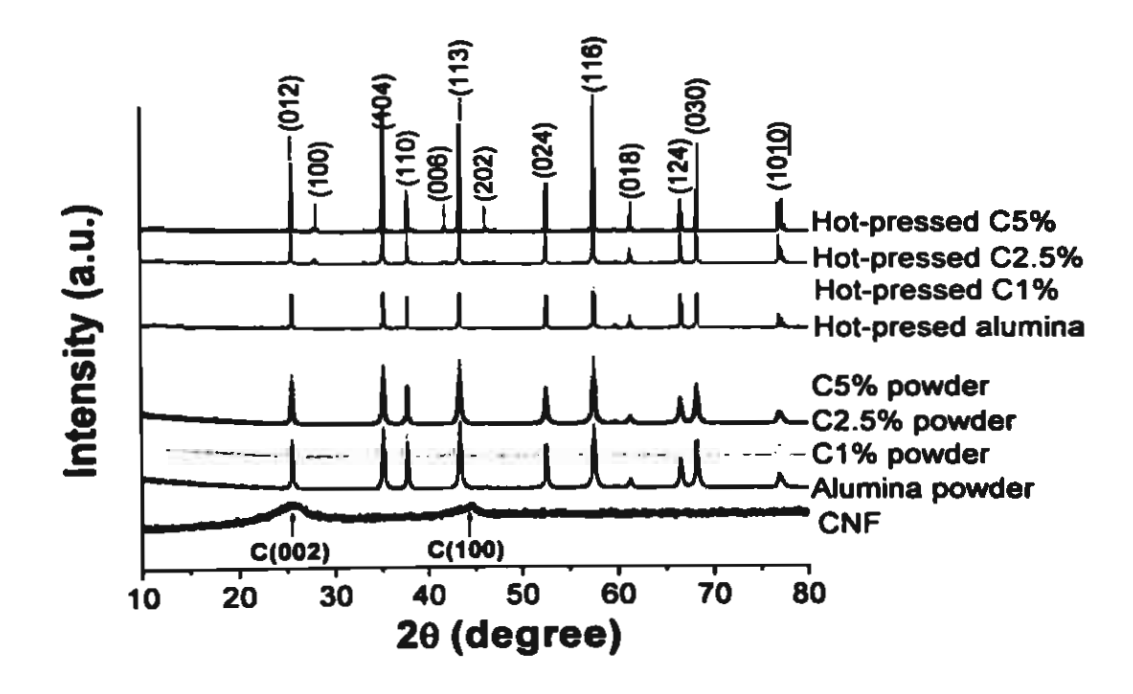


Figure 10. XRD patterns of the starting powders and hot-pressed alumina-matrix composites.

Since graphite phase of the CNF was difficult to detect by XRD, we further studied the crystal structure of the materials studied by Raman spectroscopy. The Raman spectra of the starting powders and hot-pressed materials are presented in Figure 11. Raman spectra of the alumina powder and hot-pressed alumina show typical peaks at around 380, 418, 577, 645 and 750 cm⁻¹. This is consistent with the results reported by Gallas et al. [44]. It is well-

known that the crystalline structure of graphite is well characterized by Raman spectroscopy [49, 50]. The first-order band (E_{2g2}) of single hexagonal crystal graphite in the Raman active appears at 1582 cm⁻¹ (G mode) and weak bands appear at 42 (E_{2g}) and 2724 cm⁻¹. A band around 1357 cm⁻¹ is called the D mode by disorder-induced scat scattering, which is due to imperfection or lack of hexagonal symmetry in the carbon structure, resulting in breaking the k-momentum conservation. A wide Gaussian band (M mode) is considered as an amorphous earbon contribution. Raman spectrum of the carbon nanofiber powder shows D and G peaks at around 1337 and 1590 cm⁻¹, respectively. The Raman spectrum of the C5% powder shows both alumina peaks at around 380, 418, 577, 645 and 751 cm⁻¹ and D and G peaks of CNF at 1357 and 1598 cm⁻¹. It is seen in Figure 2 that the Raman peaks of the carbon nanofiber phase are difficult to observe in the hot-pressed nanocomposite. These may be due to the oxidation/reaction of carbon nanofiber with oxygen at the surface, and also the intensities of the Raman peaks of the alumina phase are significantly high, thus hindering the two peaks of the graphite phase.

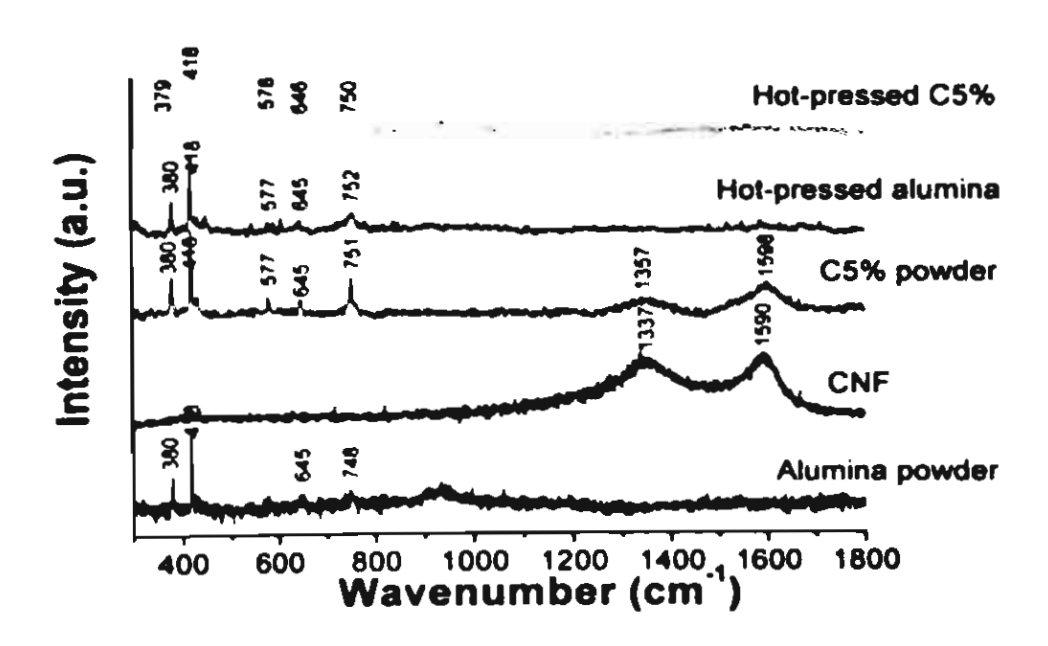


Figure 11. Raman spectra of the starting powders and hot-pressed alumina-matrix nanomposites.

2.3.2.2 Microstructure and mechanical properties

Figure 12 shows SEM micrographs of polished and thermally etched specimens. A linear intercept method has been used to evaluate the grain size of alumina and alumina/CNF nanocomposites, and the grain sizes are obtained to be 1.66 ± 0.72 , 1.19 ± 0.43 , 1.37 ± 0.45 ,

nd 1.43 ± 0.38 µm for the alumina, C1%, C2.5% and C5%, respectively. The grain sizes are ilso shown in Table 4. It is seen that all the nanocomposites have a smaller grain size than the pure alumina. This suggests that the grain growth in the nanocomposites is suppressed by CNF that pins grain boundaries. The CNF reinforcement may also play an important role in the reduction of a large scatter in grain-size distribution of the nanocomposites compared to that of the unreinforced alumina.

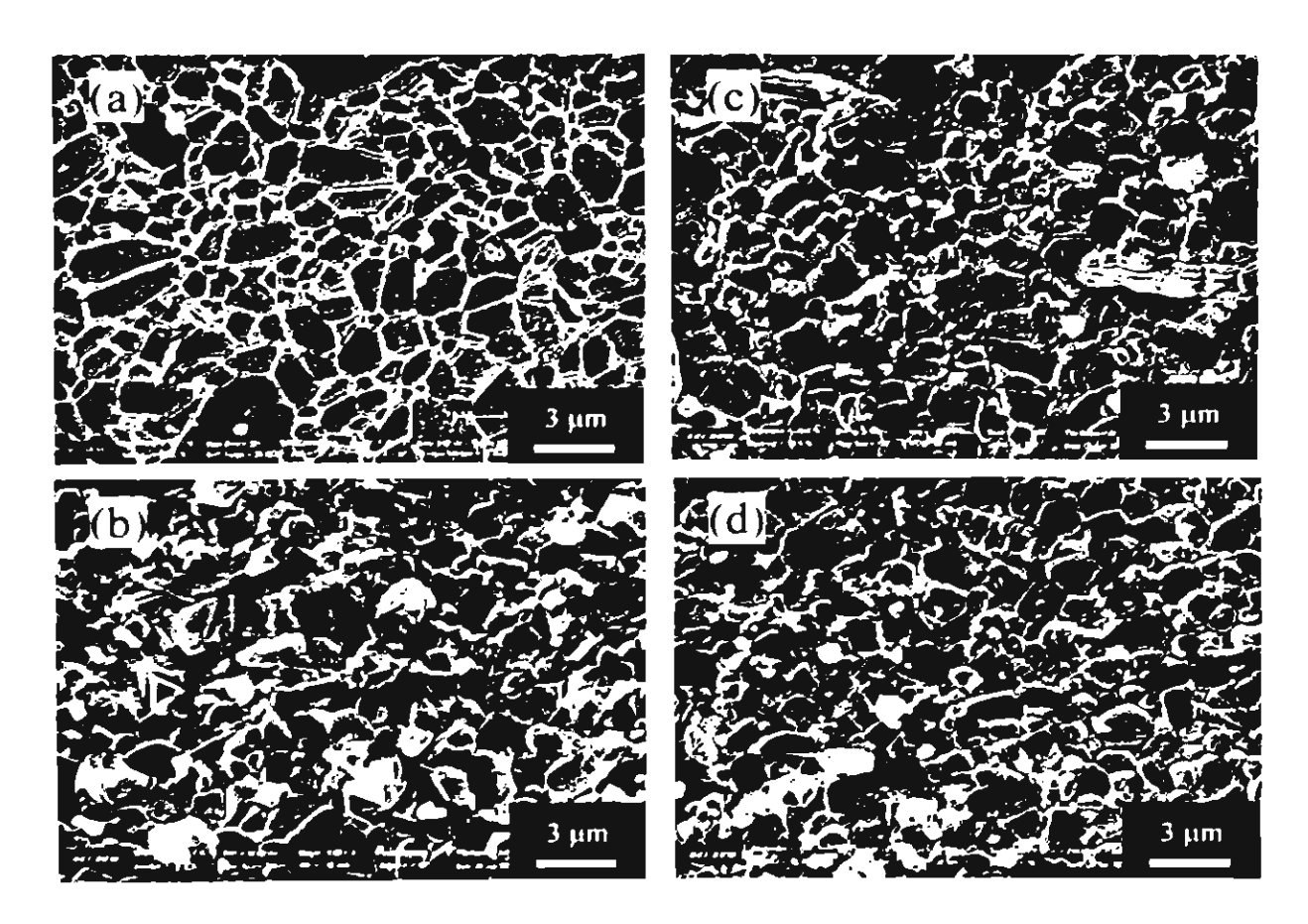


Figure 12. Microstructure of materials with different carbon nanofiber contents hot-pressed at 1450°C. (a) alumina, (b) C1%, (c) C2.5%, (d) C5%, secondary electron images.

Table 4 Summary of properties of materials investigated.

		Relative density	Grain size	Young's
Material	Symbol	(%)	(µm)	modulus
	- 41 .	00.50 . 0.05		(GPa)
Alumina	Alumina	98.73 ± 0.25	1.66 ± 0.72	370 ± 2
Alumina/1.0 vol.% CNF	C1%	98.52 ± 0.18	1.19 ± 0.43	361 ± 5
Alumina/2.5 vol.% CNF	C2.5%	99.63 ± 0.20	1.37 ± 0.45	362 ± 6
Alumina/5.0 vol.% CNF	C5%	100.00 ± 0.19	1.43 ± 0.38	340 ± 6

The relative density and Young's moduli of the hot-pressed alumina and alumina/CNF anocomposites are shown in Table 4. All the materials made in this study are almost fully lense, except pure alumina and C1% (See Table 4). The Young's modulus (E) decreases with ncreasing the amount of CNF. Although, the information about the actual value of the CNF is not available, we expect that the E of CNF used in this study is lower than that of the pure alumina and thus the low values of E in the nanocomposites would be obtained according to the strain compatibility model [46].

Figure 13 shows the fractured surface of alumina and alumina/CNF nanocomposite. The fracture mode of all the materials is predominantly intergranular. The interface between CNF and alumina matrix is strongly bonded. CNFs are reinforced on the alumina grain boundaries and seem to be wetted by the alumina matrix as shown in Figure 13(b) and Figure 13(c). However, when the volume fraction of the CNF increases up to 5.0% (C5%), some CNFs become agglomerated shown on the fractured surface of alumina-CNF nanocomposite (Figure 4(d)). These features have been found to play an important role in the low mechanical properties of carbon nanotubes reinforced alumina nanocomposites reported in Refs. [16, 20, 21].

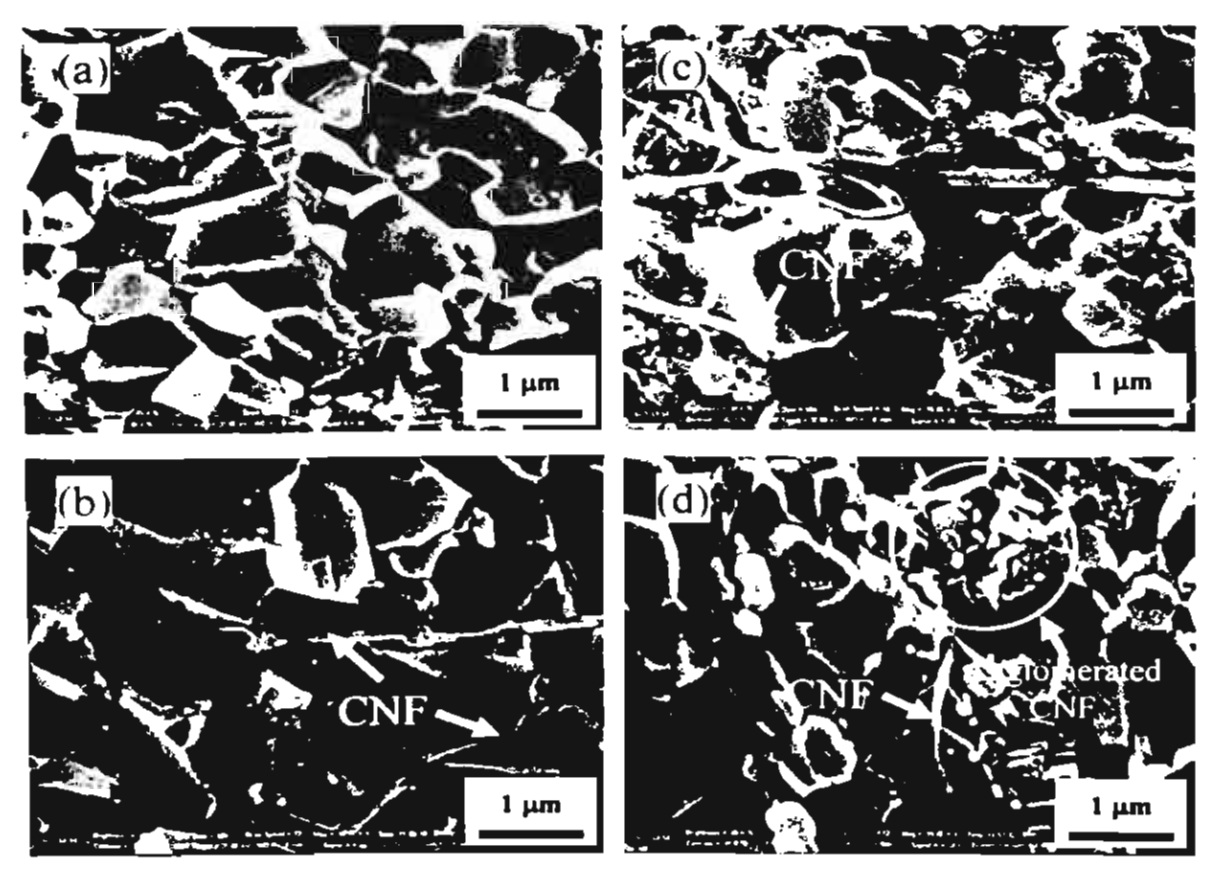


Figure 13. SEM micrographs of fracture surfaces of alumina and nanocomposite specimens. (a) alumina, (b) C1%, (c) C2.5%, (d) C5%, secondary electron images

Figure 14 shows typical well-formed 100 N contact impressions for the alumina and alumina/CNF nanocomposites tested at room temperature. The measured diagonals and radial crack lengths of each indentation were used for the calculations of hardness and fracture toughness, respectively.

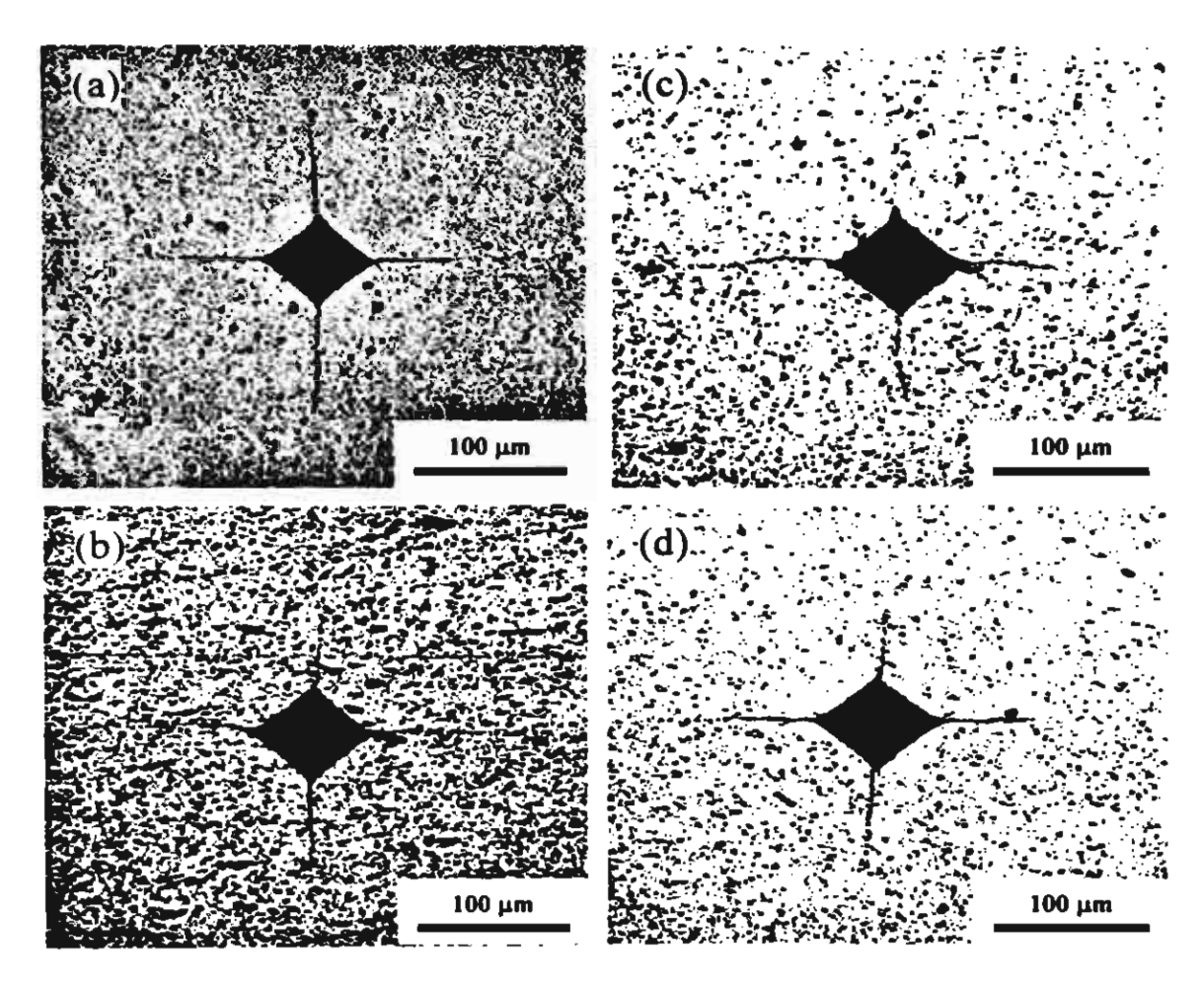


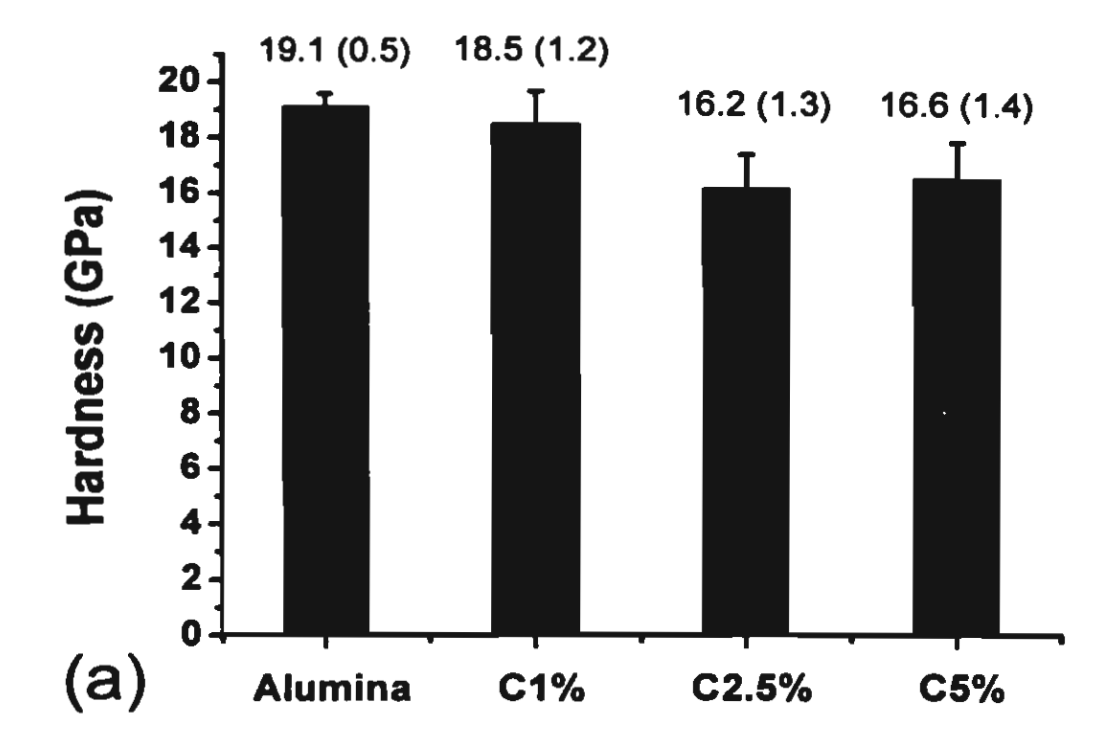
Figure 14. Optical micrographs of 50N contact impressions. (a) alumina, (b) C1%, (c) C2.5%, (d) C5%.

Hardness and fracture toughness of the materials are presented in Figure 15. It can be seen from Figure 15(a) that hardness decreases with increase the addition of CNF. On the other hand, fracture toughness (Figure 15(b)) was found to increase slightly depending on the amount of CNF. Only the increases in fracture toughness of ~ 3-5% were obtained in the C1% and C5%, whereas the highest improvement in fracture toughness of ~ 13% was observed in the C2.5%. These results are similar to the result obtained on single-walled carbon nanotube reinforced alumina-matrix nanocomposites reported by Zhan et al. [17] and on multi-walled carbon nanotubed reported by Flahaut et al. [16], which they found the decrease in hardness but increase in fracture toughness of their alumina-matrix composites with increasing the volume fraction of single-walled carbon nanotubes. However, Mo et al.

[21] reported the increase in hardness of their carbon nanotube reinforced alumina matrix nanocomposites with increasing the volume fraction of carbon nanotubes from 1.5 to 3.3 vol.%. They suggested that a difference in distribution of carbon nanotubes within the alumina matrix and interfacial strength between carbon nanotube and alumina matrix is responsible for this difference. This is because in Refs. [17] and [16] the carbon nanotubes were generally agglomerated, hence the load transfer from the matrix to carbon nanotube could not be high, but in their work the carbon nanotubes were dispersed within the alumina grains and strongly bonded with the alumina matrix. Given the evidence from fracture surface of the materials shown in Figure 13, the toughening mechanism in alumina/CNF nanocomposite in the present study can be explained by a crack bridging effect of CNF as suggested for the case of carbon nanotube reinforced alumina [19, 20]. When some carbon nanotubes are agglomerated, the fracture toughness decreases due to a decrease in crack bridging effect of CNF as observed in the C5%.

Figure 16 shows the bending strength of alumina and alumina/CNF nanocomposite before and after annealing at 1300°C for 2 h in air. For unannealed samples, the strength of the alumina/CNF nanocomposites dramatically decreases with increasing CNF volume fraction. The loss in bending strength of ~27, 33, and 47% are observed in the C1%, C2.5% and C5%, respectively. The lower values of bending strength in the nanocomposites could be correlated to some differences in the microstructure. Sun et al. [51] reported that the low density and few numbers of pulled-out caused the catastrophic decrease in bending strength of their MWNT reinforced alumina. We suspect the true density of our alumina/CNF nanocomposites was lower than the measured value, because the closed pores could not be detected by the Archimedes method. This lower density and also agglomerated CNF cause the sharply decrease in bending strength of the nanocomposites.

After annealing at 1300°C in air for 2 h, decreases in the strength of ~20% and 5% (of its original value) were respectively observed in the unreinforced alumina and C1%. On the other hand, strength improvements of ~17% and 33% were found in the C2.5% and C5%, respectively. The decrease in strength of alumina with annealing has been observed by other workers and has been attributed to grain growth [52-55], whereas the increase in strength after annealing in the nanocomposite may be due to crack healing in parallel with an oxidation reaction of the CNF as observed in alumina/SiC nanocomposites [55-59], leading to a reduction in the surface flaw density and critical flaw size on annealing.



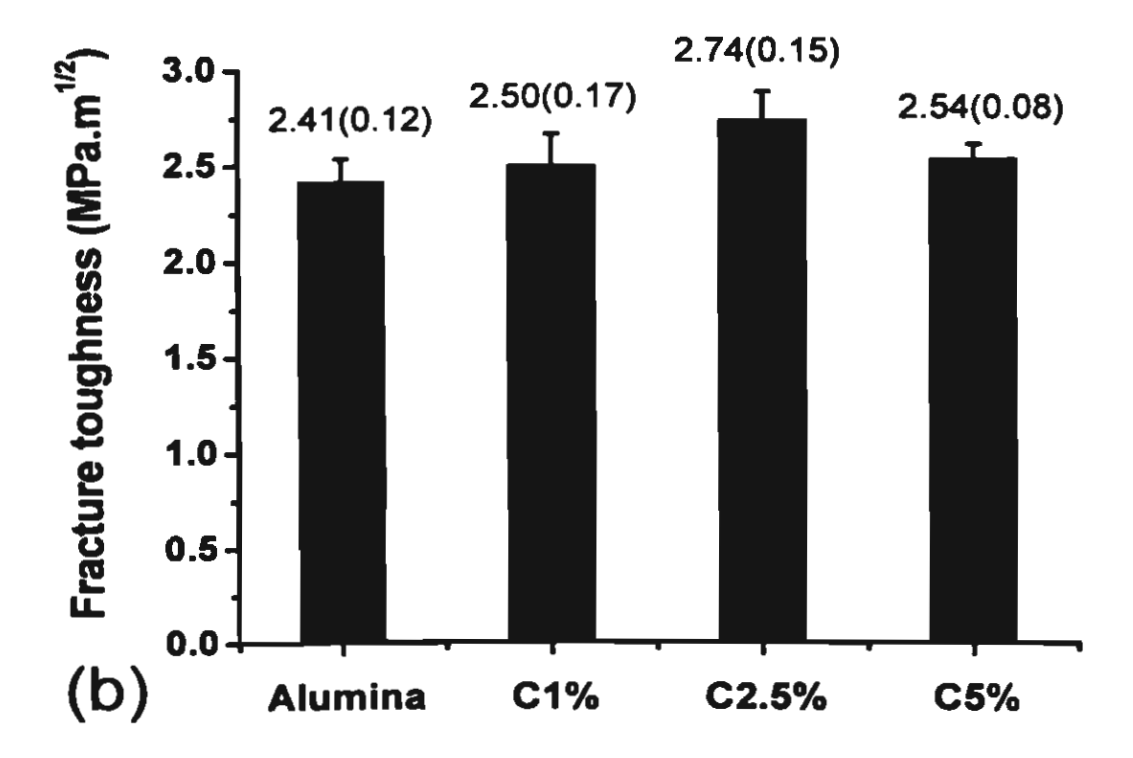


Figure 15. Indentation hardness (a) and fracture toughness (b) of alumina and aluminamatrix nanocomposites.

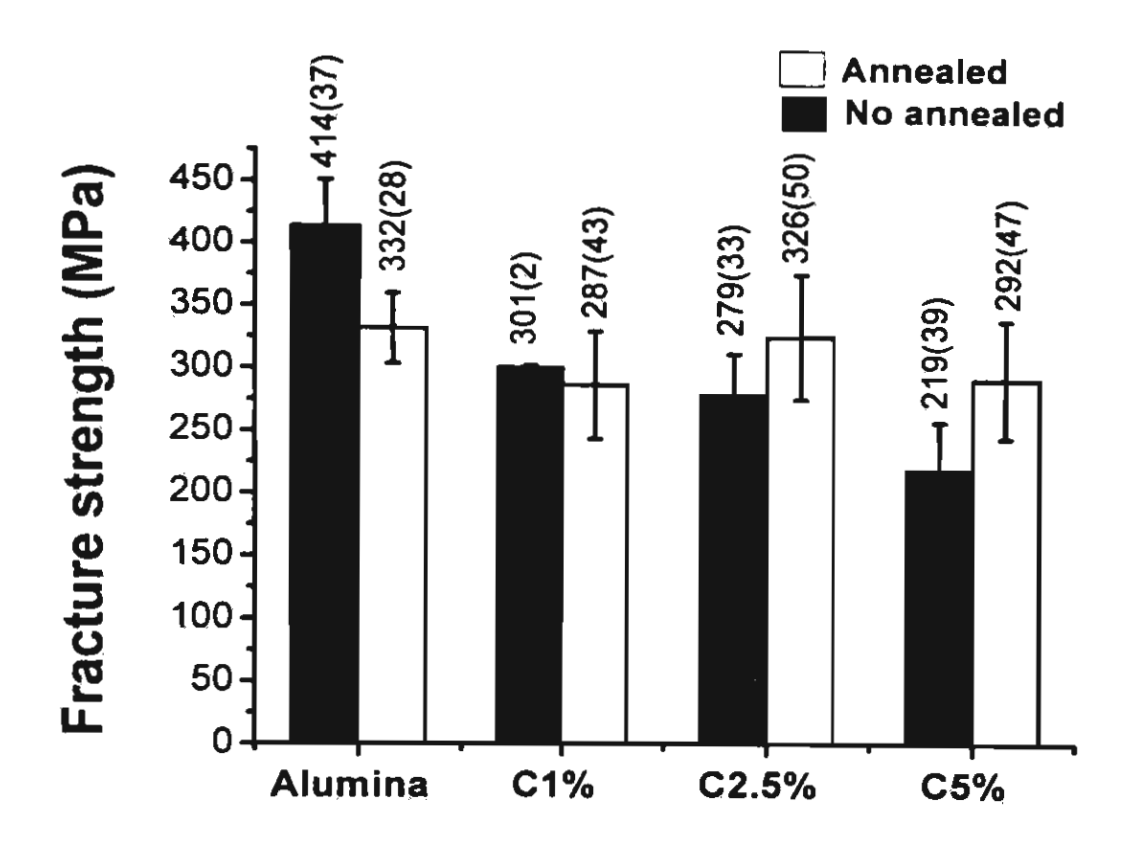


Figure 16. Room temperature 4-point bending strength of Al₂O₃ and nanocomposites before and after annealing in air at 1300°C for 2 h.

2.3.2.3 Thermoelectric power

Figure 17 shows the temperature dependence of electrical resistivity ρ for nanocomposite specimens of C2.5% and C5%. The resistivity of the C2.5% slightly decreases with increasing temperature, whereas that of the C5% dramatically decreases above 573 K. This trend may be due to the fiber-matrix interface being a barier against carrier transport as observed in carbon fiber reinforced cement reported by Wen and Chung [60]. The resistivity of both materials are very low compared to that of the alumina ($\sim 2 \times 10^9 \Omega$.cm at 773-1273 K and $> 10^{14} \Omega$.cm at $\sim 300 \text{ K}$) reported in literature [61].

Temperature dependence of Seebeck coefficient S for nanocomposite specimens of C2.5% and C5% is shown in Figure 18. The measured values range from -25 μ V/K at 300 K to -35 μ V/K at 973 K. The positive and negative values of the S indicate that these nanocomposites exhibit either p-type or n-type semiconductor behaviour depending on the measured temperatures. The positive value of S indicates electron conduction, whereas the negative value suggests predominant hole conduction in the nanocomposites [60, 62-65].

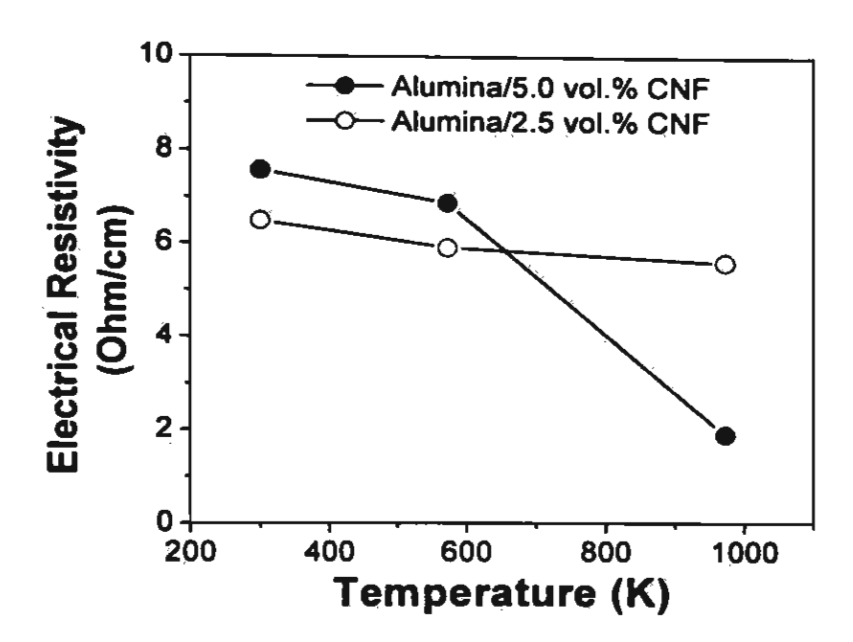


Figure 17. Temperature dependence of electrical resistivity ρ for nanocomposite specimens of C2.5% and C5%.

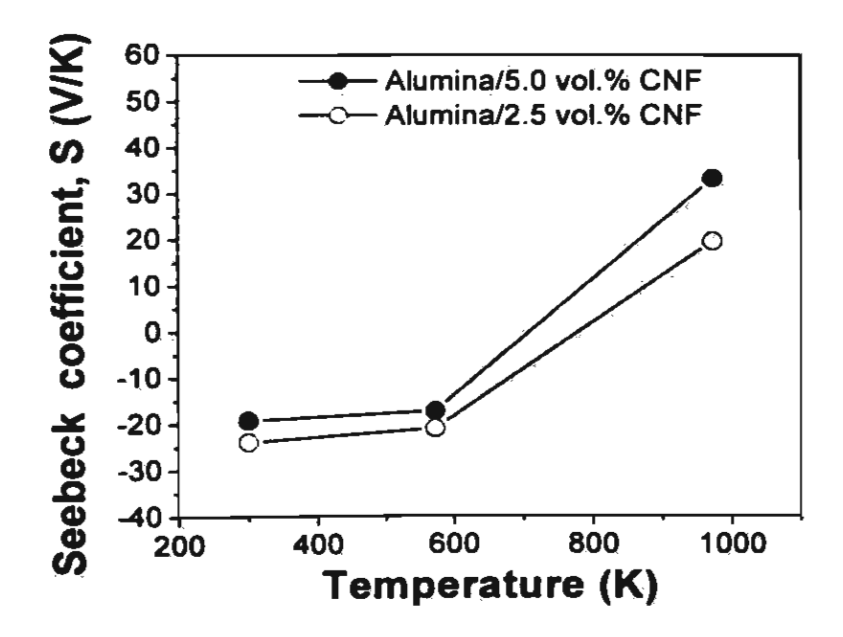


Figure 18. Temperature dependence of Seebeck coefficient S for nanocomposite specimens of C2.5% and C5%.

The thermoelectric power calculated from ρ and S values and using Eq. (10) is shown in Figure 19. P values of C5% increase with increasing temperature due to the increase in S, while those of C2.5% slightly decrease with increasing temperature due to the increase in its resistivity (decrease in electrical conductivity). It is of interest to investigate thermal